

# The secondary instability of salt fingers

By MELVIN E. STERN AND JULIAN SIMEONOV

Oceanography Department, Florida State University, Tallahassee, FL 32306-4320, USA  
stern@ocean.fsu.edu

(Received 16 July 2004 and in revised form 26 January 2005)

The primary instability of salt fingers in an unbounded fluid with uniform vertical salinity/temperature ( $\bar{S}_z^*/\bar{T}_z^*$ ) gradients consists of a vertically ( $z$ ) uniform ‘elevator’ mode, amplifying exponentially in time. We compute the  $z$ -wavelength ( $h_0$ ) of the fastest growing secondary instability by integrating a system of linear partial differential equations (PDEs) with time-dependent and horizontally periodic coefficients. It is suggested that this instability limits the amplitude of the primary mode and  $h_0\bar{S}_z^*$  determines the value of the statistically steady r.m.s. salinity fluctuation ( $S'$ ). Comparisons of  $h_0$  with  $\langle (S')^2 \rangle^{1/2}/\bar{S}_z^*$  are made using direct numerical simulations (DNS), and our theory for the vertical salt/heat flux is also given and compared with the DNS.

---

## 1. Introduction

It is well known that laminar depth ( $z$ ) independent salt fingers can be temporally amplified in an unbounded thermocline with uniform temperature gradient  $\bar{T}_z^*$  and salinity gradient  $\bar{S}_z^*$  (as conventional, the assumed constant expansion coefficients are absorbed in  $T/S$ ). Although the fastest growing disturbance, the so-called ‘elevator’ mode, satisfies the full nonlinear Boussinesq equations, it is unstable to disturbances which vary with  $z$  (Holyer 1984). In the two-dimensional case, this secondary instability has the form of a horizontal shear flow, such that the subsequent nonlinear evolution might cause adjacent fingers to merge, thereby limiting the finger amplitude and leading to the ultimate statistically steady state. Shen (1995) verified this by direct numerical simulations (DNS) of the Boussinesq equations, and another numerical example is presented in figure 1. Stern, Radko & Simeonov (2001) have also obtained results similar to figure 1, along with evaluations of the heat and salt flux which were in good agreement with ocean observations (St Laurent & Schmitt 1999). A simple explanation of the statistically steady results, and its extension to three dimensions, is the purpose of this paper.

Our discussion of the secondary instability in the present heat–salt case begins with Holyer’s (1984) linear instability calculation that, however, is limited in several respects. She assumes a basic finger state (elevator mode) with zero growth rate, rather than the one with maximum growth rate. This restriction fixes the horizontal wavelength and permits an arbitrary amplitude for the vertical velocity  $W_0(x)$  of the fingers. The amplification of  $z$ -dependent perturbations is then obtained using Floquet theory. However, the amplitude  $W_0(x)$  of the elevator mode is not ‘given’, but is strongly dependent on (and limited by) the amplitude of the secondary instability. This implies that the temporal evolution of the elevator and secondary modes must be considered simultaneously, as done herein. A second limitation of Holyer’s theory that follows from the zero-growth-rate assumption is its restriction to a single very large density ratio  $R \equiv \bar{T}_z^*/\bar{S}_z^* = K_T/K_S$ , where  $K_T$  is the heat diffusivity,  $K_S$  is the

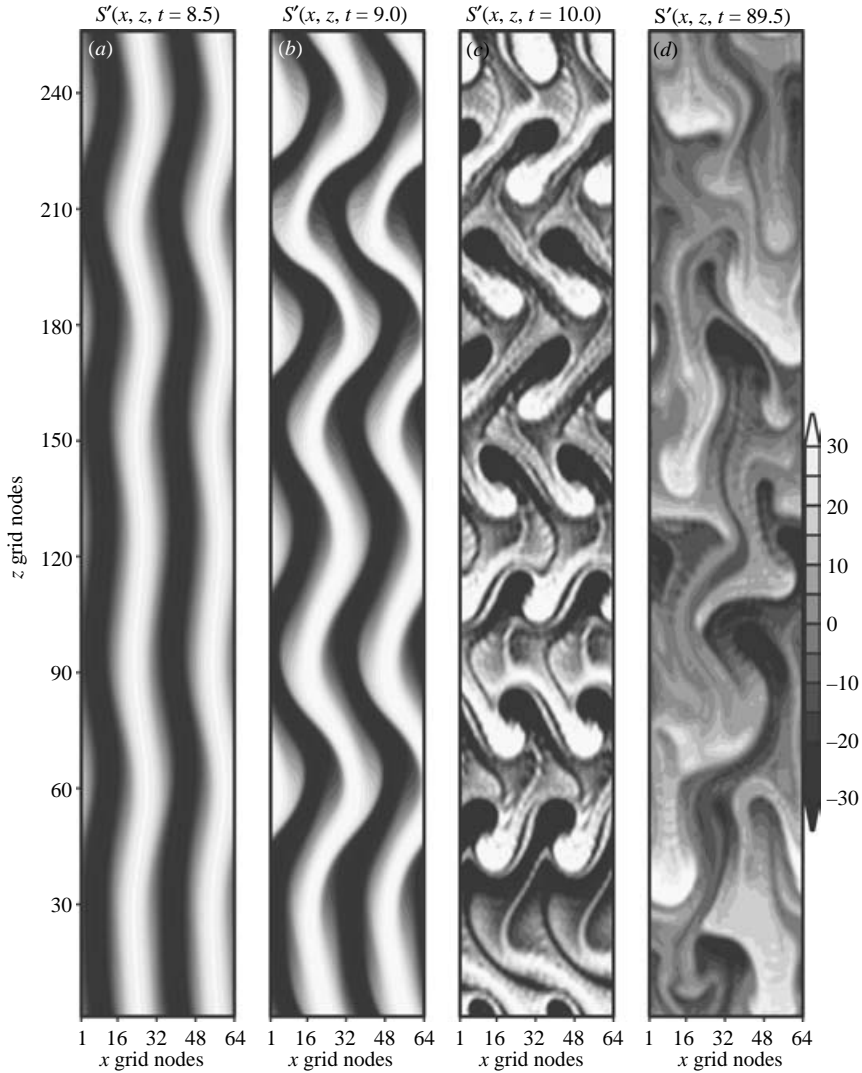


FIGURE 1. The finite-amplitude development of instability of initially straight fingers with small initial vertical velocity  $W = 2$  (see text). The disturbance isohalines illustrate the developing instability at (a)  $t = 8.5$ , (b)  $9.0$ , (c)  $10.0$ , and the final chaotic finger convection at (d)  $t = 89.5$ . To obtain this, (2.1)–(2.3) are solved for  $R = 2$ ,  $Pr = 7$ ,  $\tau = 1/24$  using the pseudo-spectral method with fourth-order Runge–Kutta time integration scheme and a time step  $\Delta t = 0.01$ . In addition to the  $z$ -independent fingers, the initial condition contained random T/S noise with amplitude  $= 0.02$ . The horizontal domain size is 2 fastest growing finger wavelengths and the vertical size is 5 times larger; the number of grid nodes is denoted on the axis.

salt diffusivity, and  $\nu$  (used subsequently) is the molecular viscosity. This  $R \simeq 10^2$  is much greater than the typical ocean value  $R \simeq 2.0$ . In this paper, we shall compute the fastest growing  $z$ -wavelength ( $h_0$ ) for different  $R$ .

In §3.2, we consider an arbitrary  $R > 1$  with the elevator mode having known values of the fastest growing wavelength (FGW) and growth rate. It is shown that this mode generates a ‘super-exponential’ growth of perturbations varying sinusoidally

with  $z$ , as determined by a system of linear partial differential equations (PDEs), with non-constant coefficients in time ( $t$ ) and in the horizontal ( $x$ ). For two-dimensional fingers with two-dimensional perturbations, the growth of the latter (as  $t \rightarrow \infty$ ) is obtained for various vertical wavelengths, and the one  $[h_0(R)]$  that grows fastest is determined. The same kind of calculation is made for three-dimensional fingers (§ 3.3) with three-dimensional perturbations by solving linear PDEs in  $(t, x, y)$ .

Section 2 indicates how these results of the linear theories for the elevator and for the secondary modes will be used to obtain an approximate explanation of some of the steady statistics in the DNS of § 4. The main assumption here is that the vertical wavelength  $h_0$  of maximum secondary growth is equal to a ‘mixing length’ for salinity  $\ell_0$ , defined in § 2. This appears plausible in the DNS of figure 1, where the amplifying  $z$ -wave (figure 1a) is seen to ‘break’ (figure 1b) and overturn, thereby producing salinity plumes (figure 1d) whose average salinity anomaly is comparable with  $\bar{S}'_z$  multiplied by the vertical wavelength. In § 4, the  $(h_0, \ell_0)$  relationship as well as our theory for the heat/salt flux will be compared with the statistics obtained in DNS.

The basic equations used in the linear/nonlinear numerics appear in § 2. A simplified explanation of the secondary instability is given in § 3.1 and the fastest growing wavelength in two/three dimensions is determined in §§ 3.2 and 3.3. Comparison with DNS appears in § 4. Alternative theories for the salt flux and eddy diffusivity are briefly discussed in the Appendix. Our results are summarized in § 5.

## 2. Basic considerations

In all the previous studies, and in what follows, the Boussinesq equations are non-dimensionalized using  $d \equiv (K_T \nu / g \bar{T}'_z)^{1/4}$  as the length unit,  $K_T/d$  as the velocity unit,  $d^2/K_T$  as the time unit, and  $\bar{T}'_z d$  as the unit for the departures ( $T, S$ ) from the basic state ( $\bar{T}'(z), \bar{S}'(z)$ ). The resulting non-dimensional equations are

$$\partial T / \partial t + \mathbf{v} \cdot \nabla T + w = \nabla^2 T, \tag{2.1}$$

$$\partial S / \partial t + \mathbf{v} \cdot \nabla S + w/R = \tau \nabla^2 S, \tag{2.2}$$

$$\nabla \cdot \mathbf{v} = 0, \tag{2.3a}$$

$$Pr^{-1} [\partial \mathbf{v} / \partial t + \mathbf{v} \cdot \nabla \mathbf{v}] = -\nabla p + \nabla^2 \mathbf{v} + (T' - S') \hat{k}, \tag{2.3b}$$

where  $\mathbf{v} = \hat{i}u + \hat{j}v + \hat{k}w$ , and  $\hat{i}, \hat{j}$  and  $\hat{k}$ , are the respective  $x, y$ , and  $z$  unit vectors;  $Pr = \nu/K_T$ , and  $\tau = K_S/K_T$ . The departure  $S = S'(x, y, z, t) + \bar{S}(z, t)$  may have a horizontally averaged component ( $\bar{S}$ ) as well as a fluctuating component  $S'$ .

Since we want to consider both two-dimensional and three-dimensional instabilities of the elevator mode, the latter will be given by

$$\hat{W}, \hat{\theta}, \hat{\sigma} = (W, \theta, \sigma) \sin k_0 x e^{\lambda t} \quad (\text{in two dimensions}) \tag{2.4a}$$

or

$$= (W, \theta, \sigma) [\cos k_0 x + \cos k_0 y] e^{\lambda t} \quad (\text{in three dimensions}) \tag{2.4b}$$

where  $W, \theta$  and  $\sigma$  are the respective amplitudes of vertical velocity, temperature and salinity. In either case (2.4a, b), the growth rate  $\lambda$  of the fastest growing wavelength ( $2\pi/k_0$ ) (see Stern 1960) satisfies the cubic

$$\lambda^3 + \lambda^2(1 + Pr + \tau)k_0^2 + \lambda[(\tau + Pr + \tau Pr)k_0^4 + Pr(1 - 1/R)] + Pr\tau k_0^6 + Pr\tau k_0^2 - Prk_0^2/R = 0, \tag{2.5}$$

and is obtained by maximizing the real root of (2.5) with respect to  $k_0$ . The fastest growing wavelength is in units of  $d$ . The modal amplitudes are related by

$$\theta = -W/(\lambda + k_0^2), \quad \sigma = -W/(R(\lambda + \tau k_0^2)). \quad (2.6)$$

Although the final amplitudes of  $(w, S', T')$  are not yet determined, their ratios may be approximated using (2.6); e.g. for the important heat/salt flux ratio we have

$$\gamma \equiv \frac{\langle wT' \rangle}{\langle wS' \rangle} \approx \frac{\langle W\theta \rangle}{\langle W\sigma \rangle} = \frac{R(\lambda + \tau k_0^2)}{(\lambda + k_0^2)}, \quad (2.7)$$

where ('bar', 'angle brackets') is the respective (horizontal, vertical) average. Equation (2.7) has previously been used (Schmitt 1979) as an approximation to the fully nonlinear and statistically steady value of  $\gamma$ . This will be verified by comparison with DNS (§ 4).

By using the subscript zero to denote dimensional quantities, the statistically steady salt flux is

$$\langle \overline{w_0 S'_0} \rangle = (K_T/d)(\bar{T}_z^* d) \langle \overline{w S'} \rangle = K_T \bar{T}_z^* \langle \overline{w S'} \rangle, \quad (2.8)$$

the salinity variance is

$$\langle (\overline{S'_0})^2 \rangle = (\bar{T}_z^* d)^2 \langle (\overline{S'})^2 \rangle, \quad (2.9)$$

and the eddy salt diffusivity is

$$D_S \equiv \frac{-\langle \overline{w_0 S'_0} \rangle}{\bar{S}_z^*} = \frac{-\langle \overline{w_0 S'_0} \rangle \langle (\overline{S'_0})^2 \rangle}{\langle (\overline{S'_0})^2 \rangle \bar{S}_z^*} = \frac{-\langle \overline{w_0 S'_0} \rangle}{\langle (\overline{S'_0})^2 \rangle} \ell_0^2 \bar{S}_z^*, \quad (2.10)$$

where

$$\ell_0 = \langle (\overline{S'_0})^2 \rangle^{1/2} / \bar{S}_z^* \quad (2.11a)$$

is a defined salinity mixing length. There is also a ' $T$ -mixing length' which is somewhat different insofar as the numerator contains  $T'_0$  and the denominator is  $\bar{T}_z^*$ . Because the finger plumes in figure 1 lose their heat anomaly much more rapidly than their salt anomaly, the ' $T$ -mixing length' should be smaller than  $\ell_0$ , and therefore is not the best measure of the maximum penetration depth of the finger blobs in the statistical state.

Our first assumption is that the wavelength of the fastest growing secondary instability  $h_0$  and  $\ell_0$  are approximately equal:

$$h_0 \cong \ell_0 \quad \text{or} \quad h \cong \ell, \quad (2.11b)$$

where  $\ell \equiv \ell_0/d$  and  $h \equiv h_0/d$  are the corresponding non-dimensional wavelengths; note that  $h$  is the same for  $T'$  and  $S'$ . We also need to evaluate

$$\frac{\langle \overline{w_0 S'_0} \rangle}{\langle (\overline{S'_0})^2 \rangle} = \frac{K_T}{d^2 \bar{T}_z^*} \frac{\langle \overline{w S'} \rangle}{\langle (\overline{S'})^2 \rangle}. \quad (2.12)$$

Equation (2.10) then becomes

$$D_S/K_T = \frac{C(R)}{R} \left( \frac{\ell_0}{d} \right)^2, \quad (2.13)$$

where  $R = \bar{T}_z^*/\bar{S}_z^* > 1$ ,

$$C(R) = \frac{-\langle \overline{w S'} \rangle}{\langle (\overline{S'})^2 \rangle} \equiv b \frac{\langle \overline{w^2} \rangle^{1/2}}{\langle (\overline{S'})^2 \rangle^{1/2}}, \quad (2.14a)$$

and  $0 \leq b \leq 1$  is the correlation coefficient between vertical velocity and salinity. Since  $S'_0 = S'T^*_z d$ , equation (2.11a) becomes:

$$\langle S'^2 \rangle^{1/2} = \frac{\ell}{R} \cong \frac{h}{R}. \tag{2.14b}$$

In §4 DNS for the left-hand side of this will be compared with values for the right-hand side obtained from the secondary instability.

With (2.7) as a precedent, we also assume that the ratio of the r.m.s. vertical velocity to the r.m.s. salinity in (2.14a) may be approximated by the linear theory (cf. (2.4) and (2.6)) for the fastest growing elevator mode; also  $b \approx 1$  is assumed. Then  $C(R) \cong |W|/|\sigma|$ , or

$$C(R) \cong R(\lambda + \tau k_0^2). \tag{2.15}$$

When (2.11b) and (2.15) are used in (2.13) we find the approximation

$$D_S/K_T \cong (\lambda + \tau k_0^2)(h_0/d)^2, \tag{2.16a}$$

where the maximum  $\lambda$  and  $k_0$  are computed from the cubic (2.5), and the value of  $h_0$  is computed from the secondary instability (§3). Using (2.7) and (2.16a), the heat finger diffusivity is:

$$\frac{D_T}{K_T} \equiv \frac{\gamma D_S}{R K_T} \cong \frac{(\lambda + \tau k_0^2)^2 h_0^2}{(\lambda + k_0^2) d^2}. \tag{2.16b}$$

The DNS in §4 will allow a comparison of the statistical results with the above theoretical approximations.

For the secondary stability problem,  $\hat{W}$ ,  $\hat{\theta}$  and  $\hat{\sigma}$  in (2.4) give the basic state, and double primes denote the perturbation. Thus in three dimensions, the equations (2.1)–(2.3), linearized about the basic state (2.4), give

$$Pr^{-1} \left( \frac{\partial}{\partial t} + \hat{W}(x, y, t) \frac{\partial}{\partial z} \right) \mathbf{v}'' + Pr^{-1} \hat{\mathbf{k}} \mathbf{v}'' \cdot \nabla \hat{W} = -\nabla p'' + \nabla^2 \mathbf{v}'' + \hat{k}(T'' - S''), \tag{2.17}$$

$$\nabla \cdot \mathbf{v}'' = \frac{\partial u''}{\partial x} + \frac{\partial v''}{\partial y} + \frac{\partial w''}{\partial z} = 0, \tag{2.18}$$

$$\left( \frac{\partial}{\partial t} + \hat{W} \frac{\partial}{\partial z} \right) T'' + u'' \frac{\partial \hat{\theta}}{\partial x} + v'' \frac{\partial \hat{\theta}}{\partial y} + w'' = \nabla^2 T'', \tag{2.19}$$

$$\left( \frac{\partial}{\partial t} + \hat{W} \frac{\partial}{\partial z} \right) S'' + u'' \frac{\partial \hat{\sigma}}{\partial x} + v'' \frac{\partial \hat{\sigma}}{\partial y} + \frac{w''}{R} = \tau \nabla^2 S'', \tag{2.20}$$

and the pressure

$$\nabla^2 p'' = \frac{\partial}{\partial z}(T'' - S'') - 2Pr^{-1} \left( \frac{\partial \hat{W}}{\partial x} \frac{\partial u''}{\partial z} + \frac{\partial \hat{W}}{\partial y} \frac{\partial v''}{\partial z} \right),$$

is computed by applying  $\nabla \cdot$  to (2.17) and using (2.18). In two dimensions (§3.2) we use (2.4a)  $\partial \hat{\theta} / \partial y = 0 = \partial \hat{\sigma} / \partial y = v'$ ; and (2.17) is replaced by the vorticity equation

$$\left( \frac{\partial}{\partial t} + \hat{W} \frac{\partial}{\partial z} - Pr \nabla^2 \right) \nabla^2 \psi'' - \frac{\partial \psi''}{\partial z} \frac{\partial^2 \hat{W}}{\partial x^2} = Pr \frac{\partial}{\partial x}(T'' - S''), \tag{2.21}$$

with  $w'' = \psi''_x$  and  $u'' = -\psi''_z$ . The (two-dimensional, three-dimensional) ‘normal modes’

are, respectively,

$$[T'', S'', \psi''] = [T_m(x, t), S_m, \psi_m]e^{imz}, \tag{2.22a}$$

$$[T'', S'', \mathbf{v}''] = [T_m(x, y, t), S_m, \mathbf{v}_m]e^{imz}. \tag{2.22b}$$

### 3. Linear theory of the secondary instability

#### 3.1. Qualitative explanation of the super-exponential growth rate

Consider first a basic finger state with purely vertical velocities  $W_3(x, t)$  which amplify according to

$$\frac{\partial W_3}{\partial t} = \lambda W_3. \tag{3.1}$$

Now subject this elevator mode to an infinitesimal amplitude perturbation consisting of a vertically varying shear flow  $U(z, t)$ , and assume this deflects the elevator mode through a small angle  $\phi(z, t)$ , thereby producing a fluctuating horizontal velocity  $u' \simeq W_3\phi$ . On kinematical grounds, we assume

$$\frac{\partial \phi}{\partial t} \simeq \frac{\partial U}{\partial z}. \tag{3.2}$$

The linearized horizontally averaged momentum equation  $\partial U/\partial t + \partial/\partial z \overline{u'W_3} = Pr\partial^2 U/\partial z^2$  then becomes

$$\left. \begin{aligned} \frac{\partial}{\partial t} U_z + \frac{\partial^2}{\partial z^2} \overline{u'W_3} &= Pr \frac{\partial^2}{\partial z^2} U_z, \\ \frac{\partial^2 \phi}{\partial t^2} + \frac{\partial^2}{\partial z^2} (\overline{W_3^2} \phi) &\simeq Pr \frac{\partial^2}{\partial z^2} \frac{\partial \phi}{\partial t}. \end{aligned} \right\} \tag{3.3}$$

This linear equation for  $\phi = \hat{\phi}(t) \sin mz$  yields the ordinary differential equation (ODE)

$$\frac{d^2 \hat{\phi}}{dt^2} + m^2 Pr \frac{d\hat{\phi}}{dt} - m^2 \overline{W_3^2} \hat{\phi} = 0. \tag{3.4}$$

For Holyer's (1984) case of a marginally growing elevator mode with constant  $\overline{W_3^2}$ , we obtain

$$\hat{\phi} = e^{\lambda_2 t}, \quad 2\lambda_2 = -Pr m^2 + \sqrt{Pr^2 m^4 + 4\overline{W_3^2} m^2} > 0, \tag{3.5}$$

implying that the shearflow disturbance (3.2) increases exponentially with time; the fingers thereby provide a negative viscosity. When  $m \rightarrow 0$ , this simple theory agrees with Holyer's (1984) equation (4.36), obtained from a truncation of the Floquet calculation for the secondary instability. Holyer's calculation predicts a fastest growing wavenumber  $\sqrt{2\overline{W_3^2}/(3Pr^2)}$  increasing with the amplitude of the basic-state fingers, a result also obtained by Shen (1995). Unfortunately, these results, as well as (3.5), require *a priori* knowledge of  $\overline{W_3^2}$ .

For the more realistic case of a time-dependent elevator mode (3.1), we let

$$\overline{W_3^2} = \Omega(t), \quad d\Omega/dt = +2\lambda\Omega, \tag{3.6}$$

where  $\lambda$  satisfies (2.5). Equation (3.4) may then be rewritten as

$$4\lambda^2 \Omega \frac{d}{d\Omega} \Omega \frac{d\hat{\phi}}{d\Omega} - m^2 \Omega \hat{\phi} + 2\lambda m^2 Pr \Omega \frac{d\hat{\phi}}{d\Omega} = 0, \quad \Omega(0) > 0. \tag{3.7}$$

The important qualitative property of this ODE is the asymptotic behaviour as  $t \rightarrow \infty$ . Using the WKB method with

$$\hat{\phi} = e^{G(\Omega)}, \quad G'' \ll (G')^2, \tag{3.8}$$

we obtain

$$4\lambda^2 \Omega^2 (G')^2 - m^2 \Omega + O(\Omega G') + O(G'') = 0.$$

Therefore,

$$\left. \begin{aligned} G' &\simeq \frac{m}{2\lambda} \Omega^{-1/2} + \dots, \\ G &\simeq \frac{m}{\lambda} \Omega^{1/2}. \end{aligned} \right\} \tag{3.9}$$

For fingers with initial  $\overline{W}_3(t=0) = 1$  or  $\Omega(t) = e^{2\lambda t}$  we finally obtain:

$$\phi \simeq \sin mz \exp\left\{\frac{m}{\lambda} e^{\lambda t}\right\}. \tag{3.10}$$

This means that  $U(t, z)$  has a ‘super exponential’ growth rate, so that its amplitude may be expected to rapidly ‘overtake’ the exponentially growing elevator mode, thereby leading to its buckling or breaking. This approximate theory is invalid for large  $m$  and does not resolve the fastest growing  $U$ ; we now turn to this problem.

### 3.2. The fastest growing vertical wavelength in two dimensions

We eventually want to study the normal mode ( $\sim \exp imz$ ) instability of the basic finger state (2.4a), by solving (2.21) together with the two-dimensional heat–salt equations. It is instructive, however, to first obtain a numerical solution in  $t, x$ , and  $z$  space, since this will reveal the numerical difficulties in the normal mode problem. Accordingly, we use the linearized perturbation equations ((2.21), etc.) and make a spectral calculation for the same parameters as used in figure 1. The computational box was  $2 \times 10$  FGW ( $64 \times 256$  grid), the initial finger velocity was  $W = 2.0$ , and the perturbation (real-valued) was initialized with random noise with amplitude 0.02 for  $T''(x, z, t)$ ,  $S''(x, z, t)$  and  $\psi''(x, z, t) = 0$ . As contrasted with the subsequent normal mode calculation, this spectral solution only resolves wavelengths which are integer fractions of the chosen domain size (i.e. 10, 10/2, 10/3, 10/4, 10/5, etc. FGW), and which can only crudely resolve the vertical wavelength of the fastest growing perturbation.

The perturbation salinity  $S''(x, z, t)$  at three different times (figure 2) shows that after the initial transient period ( $t < 5$ , not shown) the small-amplitude disturbance grows extremely fast (increasing by 10 orders of magnitude over 4 time units); in comparison, the elevator mode becomes only e-times larger over 4 time units. The large perturbation growth rate represents only one aspect of the difficulties in computing the fastest growing normal mode instability. The disturbance shown on figure 2(a, b), is dominated by vertical wavelength = 10/4 = 2.5 FGW (4 dominant peaks in the vertical) in the beginning ( $t = 5.8, t = 8.8$ ). At later times ( $t = 12.8$ ), however, there are 5 dominant peaks, suggesting a transition to a shorter fastest growing wavelength = 10/5 = 2 FGW. This illustrates the difficulty in determining an unambiguous fastest growing vertical wavelength. For rough comparison, we note that the nonlinear calculation in figure 1(a, b) has four waves in the vertical.

In order to avoid the ambiguity associated with the choice of  $t$ , we define the fastest growing disturbance as the dominant one which evolves as  $t \rightarrow \infty$ . In that

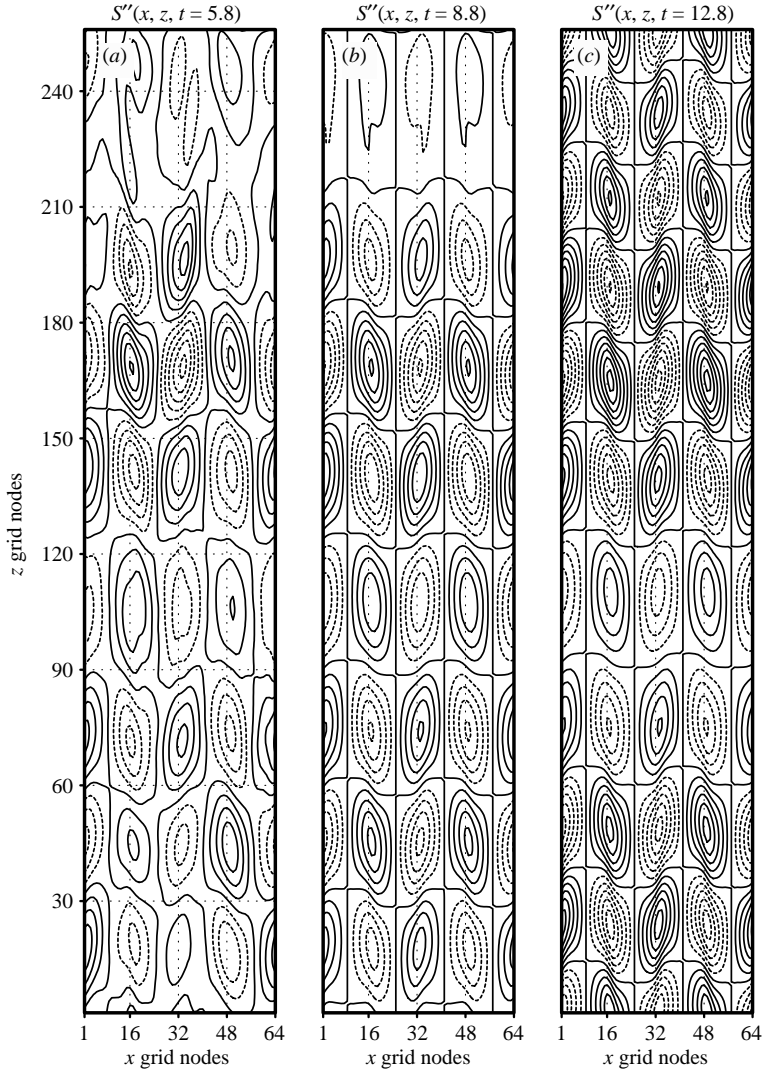


FIGURE 2. The salinity perturbation at 3 different times in the linearized two-dimensional spectral calculation for  $R=2$  and  $2 \times 10$  FGW domain. Note that the number of dominant peaks changes from 4 to 5 for  $8.8 < t < 12.8$ . The contour interval is (a) 0.01, (b) 5.0 and (c)  $5 \times 10^{10}$ .

which follows, we seek such an asymptotic length scale  $h \equiv h_0/d$  by considering the individual evolution of normal modes (2.22a) with a specified vertical wavenumber  $m$ . It is further assumed that  $T_m(x, t)$ ,  $S_m(x, t)$  and  $\psi_m(x, t)$  are horizontally periodic in an interval equal to 2 FGW, which is the same as in the spectral calculations; this domain size therefore includes the subharmonic of the elevator mode as well as the wavenumber zero. Substituting the normal modes (2.22a) in equations (2.21), etc., Fourier transforming in the horizontal and evaluating explicitly the transforms of the product terms (containing the basic elevator state) yields an ODE system (with time-dependent coefficients) of coupled equations for the Fourier components  $[\hat{T}_{km}(t), \hat{S}_{km}(t), \hat{\psi}_{km}(t)]$ . The system, truncated at a maximum horizontal wavenumber

$k = 32 \times 2\pi / (2\text{FGW})$ , has the same horizontal resolution as the aforementioned spectral calculations (64 nodes per 2 FGW) and is integrated in time using a fourth-order Runge–Kutta scheme with a time step of  $\Delta t = 0.001$ .

Our first calculation for  $R = 2$  ( $Pr = 7, \tau = 1/24$ ) was initialized with vertical velocity  $W = 2$ , and a perturbation consisting of random noise with amplitude  $10^{-10}$  for  $T_m(x, t), S_m(x, t)$ , and zero for the streamfunction  $\psi_m(x, t)$ . The foregoing spectral calculations suggest that we may restrict our search for the fastest growing perturbation to the following 13  $z$ -wavelengths:

$$2\pi/m = [1.5, 1.6, 1.7, 1.8, 1.9, 2.0, 2.1, 2.2, 2.3, 2.4, 2.5, 3.0, 4.0]\text{FGW},$$

where the finger wavelength is  $\text{FGW} = 2\pi/k_0 = 7.88$  for  $R = 2, R = 7, \tau = 1/24$ . The ODE system is solved simultaneously for all of the above modes. The growth of the different modes is compared by plotting the ratio

$$\left( \frac{\overline{T_m(x, t)T_m^*(x, t)}}{\overline{T_m(x, t - \delta t)T_m^*(x, t - \delta t)}} \right)^{1/2}, \quad \delta t = 0.2,$$

as a function of time. Figure 3(a) shows that there is no preferred wavelength at small times, but such a length scale might exist at later times. Equation (3.10) suggests a super-exponential growth rate, and to obtain the asymptotic fastest growing vertical wavelength we compute

$$G_m(t) = \ln \ln \left( \frac{\overline{T_m(x, t)T_m^*(x, t)}}{\overline{T_m(x, t - \delta t)T_m^*(x, t - \delta t)}} \right)^{1/2}, \quad \delta t = 0.2.$$

This would be a linear function of time ( $t$ ) if  $T_m(x, t) \sim \exp(\exp(at))$ , as is the case in figure 3(b) where  $G_m(t)$  is plotted (for  $t > 4$ ) for the above 13 modes. The inset on figure 3(b), showing the values  $G_m(t = 15)$  at the end of the calculation, indicates that the asymptotic fastest growing vertical wavelength is  $h = (1.7-1.8)$   $\text{FGW} = (1.75)(7.9) = 14$ . This agrees with the dominant wavelength of 2 FGW in the linearized spectral calculation (figure 2c), but is somewhat smaller than the dominant wavelength of 2.5 FGW in the nonlinear calculation (figure 1b). The consistency of the normal mode calculation is verified by the fact that the same  $h$  is obtained regardless of whether  $G_m$  is computed for temperature, salinity or horizontal velocity. The numerical accuracy of the calculation is determined from the mechanical energy equation, in which the residual term, i.e. the error in the kinetic energy power integral, remains less than 1 % of the production (and largest) term  $\langle \widehat{W} \psi'' \psi''_{xxz} \rangle$  for  $t < 11$ ; the error grows to 5 % at the end of the calculation owing to the extremely large growth rates.

To further illustrate our solution we plot the spectrum (figure 3c, d) of the horizontal velocity component  $\hat{u}_{km}$  (normalized by its r.m.s. value) as a function of  $k$  for the fastest growing  $h = 1.8$  FGW. At time  $t = 5$ , most of the perturbation energy is contained in the finger FGW, its subharmonic, and the  $k = 0$  mode. The subharmonic mode, however, disappears later and the solution at  $t = 15$  (figure 3d) is dominated by horizontal wavenumbers  $k = 0$  and  $k = 2\pi / (1 \text{ FGW})$ . Thus, the dominant energy transfer involves the elevator wavenumbers  $(k_0, 0)$ , and the waves  $(0, m)$  and  $(k_0, m)$ . This corresponds to those in the Holyer (1984) calculation in which the elevator mode amplifies a horizontal shear flow ( $k = 0$ ). Holyer only considered a marginally growing elevator mode at very large  $R = 1/(2\tau) = 50$ , and our calculation extends the theory to small  $R = 2$  and the fastest growing fingers. When this calculation was repeated for two other initial finger velocities ( $W = 0.2$  and  $W = 0.002$ ) it gave the

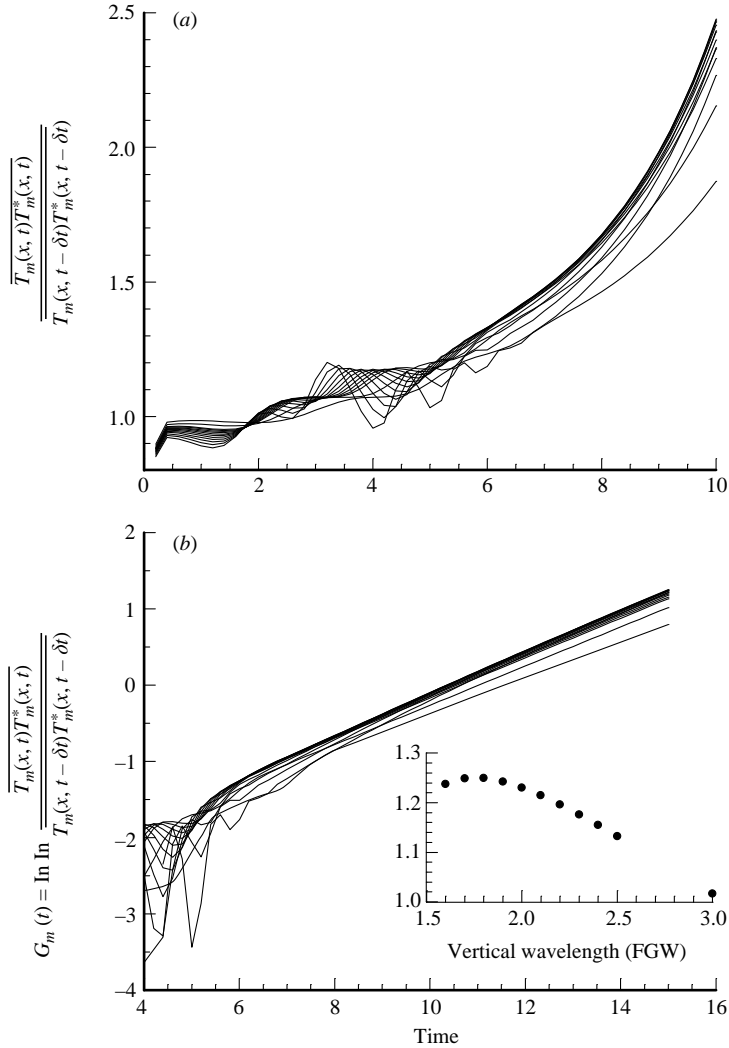


FIGURE 3(a, b). For caption see facing page.

same fastest growing wavelength of  $h = 1.8$  FGW; this verifies that the vertical length scale is independent of the initial  $W$  for sufficiently small values of the latter. Similar calculations of  $h$  for different density ratios were made and the results are given in table 1. It is seen that  $h_0/d$  increases as the density ratio approaches  $R = 1$ , but it is remarkable that the ratio of  $h$  to the finger FGW (also a function of  $R$ ) seems to remain constant. Also given in the table is the value of  $C(R)$ , computed from (2.15) and (2.5), and this decreases as  $R$  increases.

### 3.3. Three-dimensional fingers

We now want to see if the fastest growing instability of three-dimensional fingers has a vertical wavelength that differs from the value in the previous section. The basic finger state will be restricted to an elevator mode (2.4b) with a square horizontal planform, and the perturbations (2.22b) are assumed to be periodic in  $x, y$  with a period 2 FGW (this includes the finger subharmonic). The resulting linear ODE system for the Fourier coefficients  $[\hat{u}_{klm}(t), \hat{v}_{klm}(t), \hat{w}_{klm}(t), \hat{p}_{klm}(t), \hat{T}_{klm}(t), \hat{S}_{klm}(t)]$  is

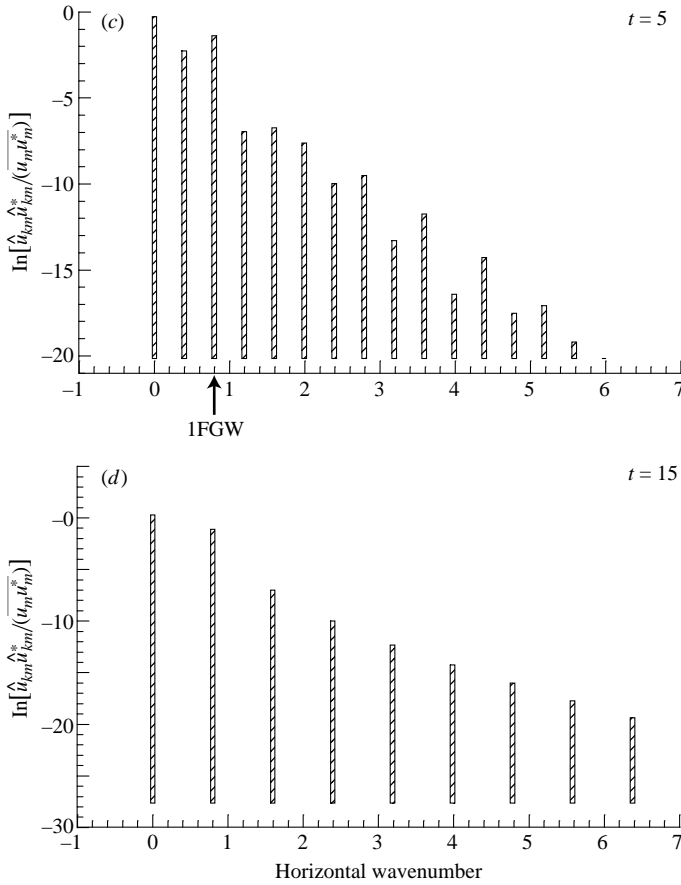


FIGURE 3. (a) Growth rates as a function of time for the 13 modes in the first linear stability calculation for  $R = 2.0$ . The growth rates are measured by the increase of the amplitude over a fixed time interval  $\delta t = 0.2$ . (b) Same as (a) except that the super-exponential trend is removed by plotting double  $\ln$  of the temperature amplitudes; shown are later times than those in (a). The linear trend indicates that the calculation reached an asymptotic solution. The inset shows  $G_m(t = 15)$  as a function of the vertical wavelength. (c, d) Bar charts of the normalized horizontal velocity spectrum for the fastest growing wavelength 1.8 FGW in (b). The horizontal wavenumber corresponding to 1 FGW is also indicated. Note that the base of the vertical bars does not extend to the zero ordinate ( $-\infty$  on the logarithmic scale), but is cut off at some arbitrary level. Half of the harmonics in (c) disappear in (d) because their amplitude is smaller than the cutoff level.

truncated at horizontal wavenumbers  $k = l = 32 \times 2\pi / (2 \text{ FGW})$ . The fastest growing wavelength is then determined by time integration of the ODE system for each of the following vertical wavelengths:

$$2\pi/m = [1.9, 2.0, 2.1, 2.2, 2.3, 2.4, 2.5, 2.6, 2.7, 2.8, 2.9, 3.0] \text{FGW},$$

where FGW as a function of the density ratio is given in table 1 and repeated in table 2.

The first three-dimensional linear calculation was for  $R = 1.5$ ,  $Pr = 7$ ,  $\tau = 1/24$  with an initial amplitude of the fingers, (2.4b), corresponding to  $W = 2$ . As previously, the initial perturbation velocities are zero, whereas  $T_m(x, y, t)$  and  $S_m(x, y, t)$  are initialized using small-amplitude ( $10^{-10}$ ) random noise; the time step for the numerical

$R$	1.0	1.25	1.5	2.0	2.5	3.0
FGW	12.4	9.31	8.47	7.88	7.68	7.60
$h_0/d$	21.1	15.8	14.4	14.1	13.8	13.7
$h_0/(\text{FGW} \times d)$	1.7	1.7	1.7	1.8	1.8	1.8
$\lambda(R)$	0.705	0.485	0.372	0.251	0.187	0.146
$\gamma(R)$	0.744	0.670	0.643	0.627	0.626	0.631
$C(R)$	0.716	0.630	0.593	0.556	0.536	0.524
$\ell_0/d$	—	$29.2 \pm 1.4$	$23.9 \pm 1.3$	$22.1 \pm 1.3$	$20.8 \pm 1.3$	$19.7 \pm 0.8$
$\gamma_{DNS}$	—	$0.68 \pm 0.05$	$0.66 \pm 0.05$	$0.63 \pm 0.05$	$0.61 \pm 0.03$	$0.61 \pm 0.02$
$C_{DNS}$	—	$0.23 \pm 0.03$	$0.24 \pm 0.03$	$0.24 \pm 0.03$	$0.24 \pm 0.03$	$0.24 \pm 0.03$

TABLE 1. The non-dimensional vertical wavelength  $h_0/d$  of the asymptotic fastest growing secondary instability (two-dimensional) and the wavelength of the fastest growing elevator mode for different density ratios,  $Pr=7$ ,  $\tau=1/24$ . The growth rate  $\lambda$  in (2.5), the theoretical flux ratio  $\gamma$  (2.7) and the coefficient  $C$  in (2.15), computed for the fastest growing wavenumber  $k_0=2\pi/\text{FGW}$ . Also given at the bottom of the table are the non-dimensional ‘mixing’ length  $\ell_0/d$ ,  $\gamma_{DNS}=\langle \overline{wT'} \rangle / \langle \overline{wS'} \rangle$  and  $C_{DNS}=-\langle \overline{wS'} \rangle / \langle (\overline{S'})^2 \rangle$  as obtained from the DNS of Stern *et al.* 2001. For typical thermocline  $\overline{T}_z^*$ ,  $K_T=1.5 \times 10^{-3} \text{ cm}^2 \text{ s}^{-1}$ ,  $\nu=10^{-2} \text{ cm}^2 \text{ s}^{-1}$ , the finger length scale  $d$  is about 1 cm.

$R$	1.0	1.25	1.5	2.0	2.5	3.0
FGW	12.4	9.31	8.47	7.88	7.68	7.60
$h_0/d$	28.5	21.4	19.5	18.1	17.7	17.5
$h_0/(\text{FGW} \times d)$	2.3	2.3	2.3	2.3	2.3	2.3
$C(R)$	0.716	0.630	0.593	0.556	0.536	0.524

TABLE 2. The vertical wavelength  $h_0$  of the fastest growing three-dimensional secondary instability for different density ratios,  $Pr=7$ ,  $\tau=1/24$ . (The theoretical value of  $C(R)$  is the same as in the two-dimensional case).

integration was  $\Delta t=0.0005$ . The plot of  $G_m(t)$  in the three-dimensional run for  $R=1.5$  (figure 4) suggests that asymptotic solutions with super-exponential growth have been reached by  $t=9$ . The inset of figure 4 indicates that the asymptotic fastest growing wavelength is  $h=2.3 \text{ FGW}=18.1$ , which is about 30% larger than the corresponding two-dimensional wavelength. Although either wavenumbers  $k_x=0$  or  $k_y=0$  appear transiently in this calculation, a mean shear flow  $[(k_y, k_x)=(0, 0)]$  is not generated, as is the case in two-dimensions. Similar three-dimensional calculations for various density ratios (table 2) show that, as in the two-dimensional case,  $h$  decreases when  $R$  increases and the ratio of  $h$  to the finger FGW is also a constant, however, equal to 2.3.

## 4. Comparison with DNS

### 4.1. Two-dimensional DNS

A DNS for  $R=2$ ,  $Pr=7$ , and  $\tau=1/24$  was made in a  $2 \times 10$  FGW domain, similar to figure 1 and the linear spectral calculation in §3.2. The main difference from figure 1 is that the initial T/S perturbation to the elevator mode is random only in the horizontal and has a vertical wavelength  $=2\text{FGW}=15.8$ . This wavelength is approximately equal to the wavelength of the fastest growing secondary instability. The initial vertical velocity of the elevator mode was  $W=2$  and the perturbation salinity and temperature amplitudes were 0.02 and 0.01, respectively.

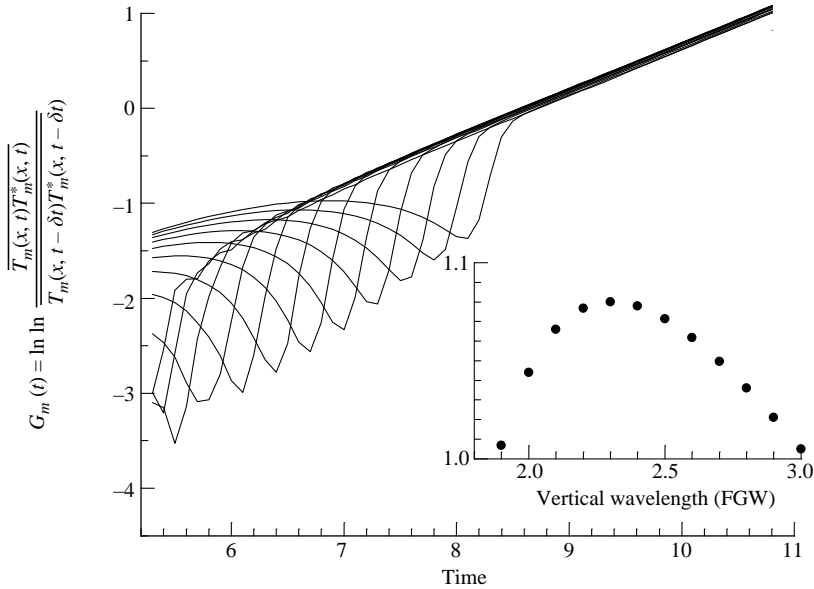


FIGURE 4. Growth rates as a function of time for 12 modes used in the three-dimensional linear stability calculation for  $R=1.5$ . Plotted is a double ln of the increase of temperature amplitude over the fixed time interval  $\delta t=0.2$ . Also shown in the inset is  $G_m(t=10.8)$  as a function of the vertical wavelength.

The evolution of the total salinity variance (figure 5a) illustrates that the growth of the elevator mode is interrupted at  $t=10$  and that the subsequent statistically steady fingers have  $\langle(S')^2\rangle^{1/2}=11.1$ ; the corresponding salt flux is  $\langle wS'\rangle = -29.7 \pm 4.5$ . This  $\langle(S')^2\rangle^{1/2}$  is about 1.6 times the predicted theoretical r.m.s. salinity  $=(h/R)=(14.4/2)=7.2$ . As will be illustrated by the solution spectra, this discrepancy is due to the presence of wavelengths longer than  $h$  in the final chaotic fingers. For example, the subharmonic of  $h$  arises because of the merger of adjacent finger blobs into larger plumes, as revealed by a movie of the finger evolution beyond the time of figure 1(c).

In considering the solution spectra, we first concentrate on the initial wave-breaking stage to show the relevance of the length scale  $h$  in the finite-amplitude phase. A plot of the salinity variance spectra at various times (figure 5b-d) illustrates that, for  $t \leq 14.5$ , the maximum amplitude is maintained at a wavenumber approximately equal to  $2\pi/h$  and there are also discrete harmonics of finite amplitude. Subsequently, in the wave-breaking stage of figure 1, other Fourier harmonics develop with finite amplitude, but wavelength  $2\pi/h$  still dominates the solution (figure 5e).

The average (from  $t=10$  to  $t=100$ ) spectrum of the statistically steady state (figure 5f) shows that vertical wavelengths longer than  $h$  also develop and that the fundamental wavelength (10 FGW) has the largest amplitude. To further examine the long waves, the calculation was continued for another 100 time units (figure 6) by periodically extending the final data in a  $4 \times 40$  FGW domain and adding to it small-amplitude (0.02) noise. This extended run had an average salt flux  $\langle wS'\rangle = -29.9 \pm 1.7$  and r.m.s. salinity  $\langle(S')^2\rangle^{1/2} = 11.2$  which agree closely with those in the small domain run (figure 5). The time average vertical spectrum of the temporally extended calculation (not plotted) shows that the spectrum becomes flat

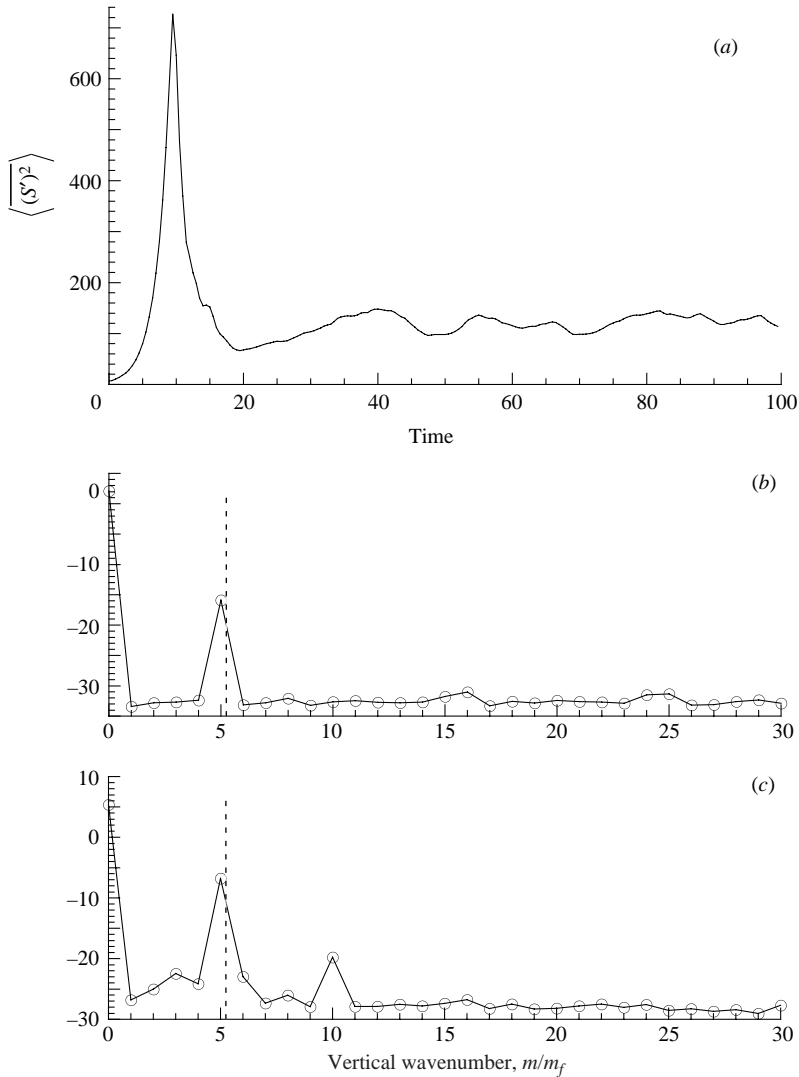


FIGURE 5(a-c). For caption see facing page.

at wavelengths longer than 10 FGW, with amplitude 3–4 times smaller than the amplitude of the fundamental wavelength in the  $2 \times 10$  FGW calculation.

A better illustration of the spectral distribution of the salinity/temperature variance in the extended calculation is provided by a variance-preserving plot (figure 6). Most of the  $S'$  energy is in waves longer than  $h$  which explains why the statistically steady  $\langle (S')^2 \rangle^{1/2}$  is greater than the prediction (2.14b) based on  $h$ . The plot shows a salinity peak at wavelength 1.5 FGW, approximately equal to  $h$ , and a temperature peak at twice that wavelength. The following tentative explanation is offered for the difference in the salinity and temperature spectra. The ratio of the salinity and temperature variance in the linear secondary instability calculation of figure 2 was about 2.7 and is almost the same as the ratio  $44/16 = 2.75$  of the salinity and temperature spectral amplitudes at wavelength  $h$  (figure 6). At wavelengths longer than  $h$ , the difference between the salinity and temperature spectral amplitudes is

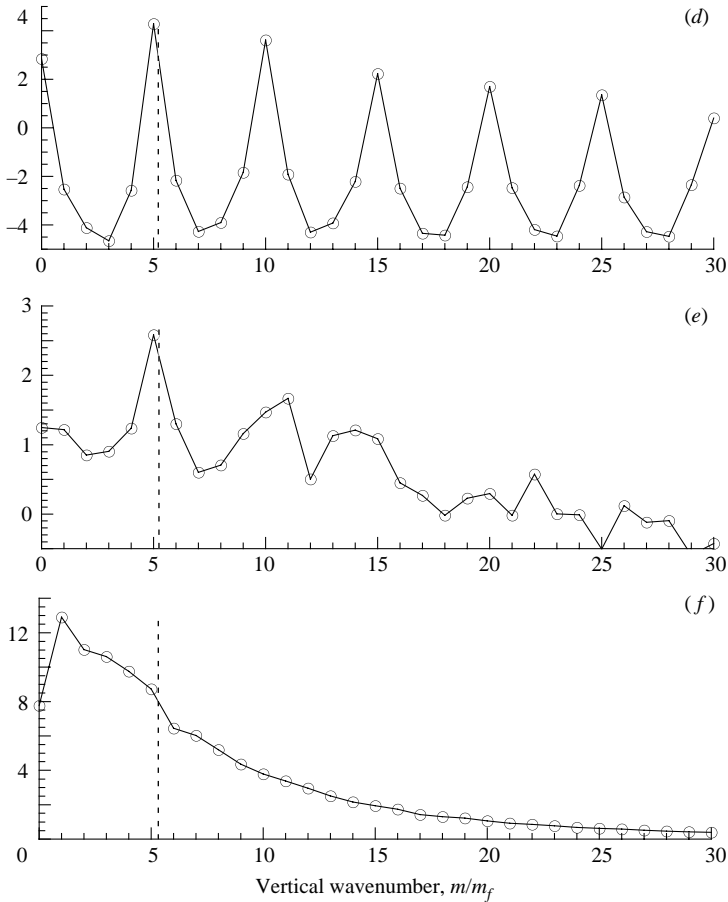


FIGURE 5. A  $2 \times 10$  FGW calculation for  $R = 2$ ,  $Pr = 7$ ,  $\tau = 1/24$  similar to the one on figure 1, except that the initial perturbation contains the vertical wavelength of the fastest growing secondary instability (see text). (a) Total salinity variance as a function of time; after an initial overshoot the r.m.s. salinity levels off at  $(\overline{(S')^2})^{1/2} = 11.1$ . (b–f) Natural log of the vertical salinity spectrum,  $\ln(\sum_k \hat{S}_{km} \hat{S}_{km}^*)$ , as a function of the vertical wavenumber normalized by the  $z$ -fundamental wavenumber  $m_f$  at various times (b)  $t = 0.5$ , (c) 7.0, (d) 14.5, (e) 17.5, and (f) the time-averaged ( $10 < t < 100$ ) spectrum  $\sum_k \hat{S}_{km} \hat{S}_{km}^*$ . The dashed line denotes the wavelength of the fastest growing secondary instability.

decreased owing to vertical advection of the mean  $\bar{T}_z^*$  and  $\bar{S}_z^*$  by large-scale motions. Since  $R = \bar{T}_z^*/\bar{S}_z^* > 1$ , the temperature spectrum will most probably cross above the salinity spectrum at wavenumbers lower than those plotted on figure 6.

Similar calculations for other  $R$  (table 1) show that  $\gamma_{DNS}$  decreases slightly with  $R$  and is in good agreement with the theoretical  $\gamma$ . The DNS values of  $(\ell_o/d)$  (table 1) exceed the theoretical  $(h_o/d)$  by less than a factor of two, as in the DNS in figure 5. Since the ratio of salt flux to the salinity variance ( $C_{DNS}$ ) is smaller than the theoretical value  $C$  by a factor of two (table 1) we see that there is a compensation of the errors in the terms of (2.13) which determines  $D_S$ . This explains why the theoretical values plotted in figure 7 are in such good agreement with the DNS at various density ratios. Because the predicted  $\gamma$  (table 1) and  $D_S$  (figure 7) compare well with the DNS, the predicted heat diffusivity  $D_T$  (2.16b) will also be in good agreement with the DNS.

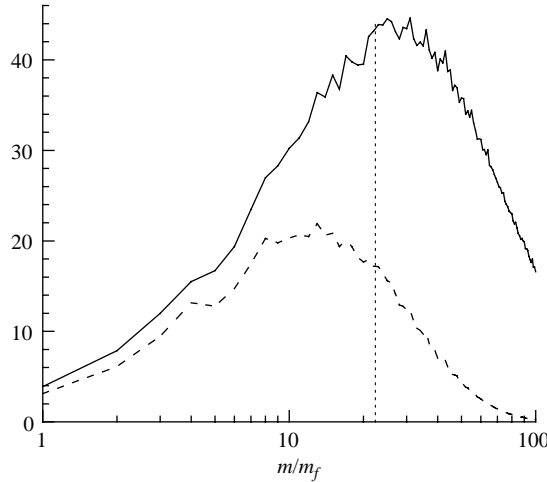


FIGURE 6. A variance-preserving plot of salinity  $(m/m_f) \sum_k \hat{S}_{km} \hat{S}_{km}^*$  (solid) and temperature  $(m/m_f) \sum_k \hat{T}_{km} \hat{T}_{km}^*$  (dashed) vertical spectra in the  $4 \times 40$  FGW calculation, extending the run in figure 5 for another 100 time units. Plotted is the time-averaged spectra, the vertical wavenumber is normalized by the  $z$ -fundamental wavenumber  $m_f$  and only modes with  $1 \leq m/m_f \leq 100$  are shown. The finger FGW corresponds to  $m/m_f = 40$  and the wavelength (1.8 FGW) of the fastest growing secondary instability is denoted by the vertical dashed line. In the statistically steady state, the salinity peak is at a wavelength ( $m^{-1}$ ) which is half that of the temperature peak.

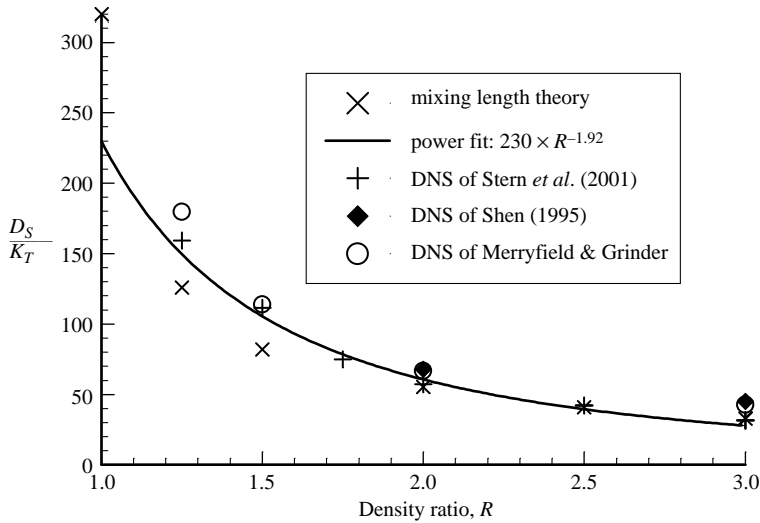


FIGURE 7. The eddy diffusivity  $D_S/K_T$  as a function of  $R$  obtained from  $\times$ , the mixing length theory, and the two-dimensional DNS of  $+$ , Stern *et al.* (2001),  $\blacklozenge$ , Shen (1995), and  $\circ$ , Merryfield & Grinder. The theoretical diffusivities ‘ $\times$ ’ are obtained from (2.16a) with  $h_0/d$  given by table 1. The solid line is a power fit to the ‘ $\times$ ’ points. The DNS of Stern *et al.* (2001) and the mixing length theory are for  $\tau = 1/24$  while in the other two DNS studies  $\tau = 0.01$ .

4.2. Three-dimensional fingers

The three-dimensional linear theory results in table 2 show that, as in the two-dimensional case, the wavelength of the fastest growing instability is proportional to the finger FGW and decreases with increasing  $R$ . Since  $C(R)$  and FGW are the same

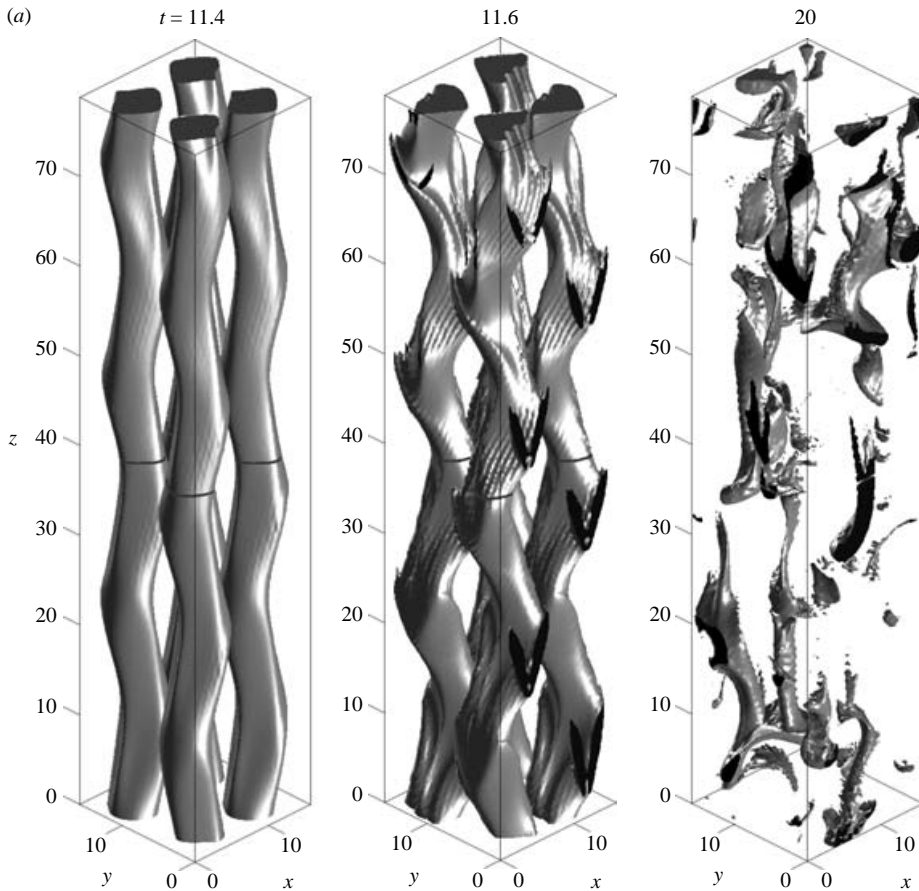


FIGURE 8(a). For caption see next page.

in two and three dimensions, our theory predicts the same power dependence  $D_S(R) \sim R^{-1.9}$  (figure 7) for both cases. Using  $h = 18.1$  for  $R = 2$  (table 2), our three-dimensional theory predicts r.m.s. salinity amplitude  $(2.14a) \langle (S')^2 \rangle^{1/2} = 18.1/2 \approx 9.1$  which is 30 % larger than the corresponding two-dimensional value. The theory (2.16) also predicts a three-dimensional salt eddy diffusivity  $D_S/K_T = 91$  which is 1.7 times larger than the corresponding two-dimensional diffusivity.

These theoretical estimates for the r.m.s. salinity and the salt flux will now be compared with a three-dimensional DNS for  $R = 2$  in a  $2 \times 2 \times 20$  FGW domain. The numerical grid had 64 nodes in  $x, y$  and 512 nodes in  $z$ , resulting in grid step  $\Delta x = \Delta y = 0.25$  and  $\Delta z = 0.31$ ; a time step  $\Delta t = 0.005$  was used for time integration. The calculation was initialized using the fastest growing vertical fingers in (2.4b) with  $W = 2$  and with small-amplitude (0.02) random noise for the horizontal velocities. Initially, the finger flux increases exponentially reaching the large value  $-2188$ , but at  $t = 11$  (figure 8b) the flux starts to equilibrate. Unlike the corresponding two-dimensional calculation (figure 1) the instability of the vertically elongated fingers in figure 8(a) does not produce an initial mean horizontal shear flow, but each finger merges with a nearby finger with the same properties at periodic vertical intervals approximately equal to 3.3 FGW.

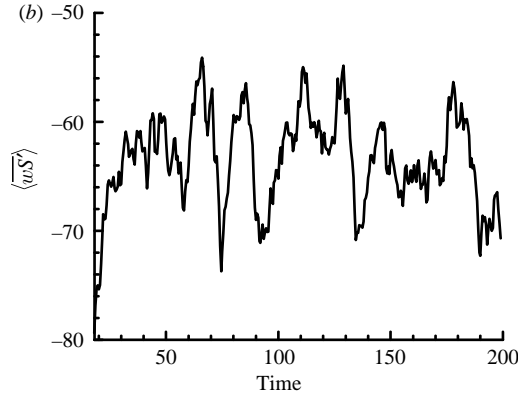


FIGURE 8. (a) Volumetric plot of the  $S'(x, y, z) = 25$  salinity isosurface in the three-dimensional spectral calculation for  $R = 2$ ,  $Pr = 7$ ,  $\tau = 1/24$  in  $2 \times 2 \times 20$  FGW domain; shown is only the lower half of the domain  $0 < z < 10$  FGW = 78. The first two panels (for  $t = 11.4$  and  $t = 11.6$ ) illustrate the finger instability and the third panel illustrates the subsequent chaotic convection. Grey shading denotes the  $S' = 25$  isosurface and black corresponds to the isosurface interior  $S' > 25$  which is visible at cross-sections of the isosurface  $S' = 25$  with the walls. Note the developing large-scale structure at  $t = 20$ . (b) Average salt flux as a function of time in the three-dimensional spectral calculation for  $R = 2$ . The large peak  $\langle wS' \rangle = -2188$  at  $t = 11$  is not shown.

The r.m.s. salinity  $\langle (S')^2 \rangle^{1/2} = 14$  in the above three-dimensional DNS is about  $14/9.1 = 1.5$  times larger than the predicted value. As in the two-dimensional case, the difference between  $\ell_0$  and the prediction  $h_0$  (table 2) is again explained by the generation of longer scales (figure 8a) owing to merging of finger blobs. The statistically steady value  $C(R) = 0.32 \pm 0.01$  is about half the corresponding theoretical estimate (table 2,  $R = 2$ ). As before the compensation of the errors in  $C$  and  $\ell_0$  in (2.13) brings about better agreement of the theoretical estimate of  $D_S$  with the DNS. The equilibrium salt flux  $\langle wS' \rangle = -63$  of the statistically steady fingers (figure 8b) implies a salt eddy diffusivity  $D_S/K_T = 124$ . Thus, our theory (§ 2) only underestimates the three-dimensional fluxes by about 30%. It should be noted, however, that the numerical eddy diffusivity will be slightly reduced if the horizontal domain size of the DNS is increased. For example, Stern *et al.* (2001) have shown that in a three-dimensional DNS for  $R = 2$ ,  $Pr = 7$ ,  $\tau = 1/6$  the heat flux decreases 15% when the horizontal domain size is doubled from two to four finger pairs. This can be explained by noting that in a wider domain the fingers generate larger-scale motions (on scales of several FGW), which dominate the solution and which are less efficient in transporting heat/salt in the vertical.

## 5. Conclusion

The exponential growth of the elevator mode is terminated by a secondary instability of super-exponential growth rate. The fastest growing vertical wavelength  $hd$  multiplied by  $\bar{S}_z^*$  determines a characteristic amplitude  $S'$ . This is related to a (dimensional) ‘mixing’ length:

$$R \langle (S')^2 \rangle^{1/2} d \equiv \ell d.$$

DNS calculations of  $\ell$  show that it exceeds  $h$  by a factor between 1.4 and 1.8. The discrepancy is attributed to the subharmonic of  $h$ , which is associated with the merger

of fingers to form plumes. To predict the salt flux we also need to consider the factor  $C$  (equation (2.14a)) which is the product of  $\text{r.m.s.}(w)/\text{r.m.s.}(S')$  and the correlation coefficient between  $w$  and  $S'$ . It is assumed that the elevator mode can be used to evaluate  $C$  in the statistically steady state. DNS calculations show that the result is again in error by a factor  $\sim 2$ , but fortunately the errors in  $C$  and  $\ell$  compensate in determining the salt flux, which agrees with the DNS (figure 7). A useful formula (equation (2.16)) for the eddy heat/salt diffusivities is thereby obtained.

When the secondary stability problem was solved in three dimensions we obtained (table 2) an  $h$ , which is 30% larger than in two-dimensions. For  $R=2$ , our theory (2.16) predicts a salt flux which is 1.7 times larger than the corresponding two-dimensional value. Similarly, the equilibrium three-dimensional DNS flux (figure 8b) is 2.1 times larger than the two-dimensional flux for the calculation in figure 5. Stern *et al.* (2001) also found three-dimensional finger fluxes that are about 2–2.5 times larger than the corresponding two-dimensional fluxes in DNS for  $R=2$  and  $\tau=1/6$ ,  $\tau=1/12$ . Thus, our mixing-length theory is able to explain the increase of the finger fluxes in three-dimensional DNS.

The mechanism for limiting the growth of fingers in the heat–salt case considered here is similar to that found by Stern & Simeonov (2004) for the sugar–salt case (much larger  $\tau$  and  $Pr$ ). Using a mode truncation of the nonlinear T/S equations (with negligible inertial terms), these authors show that the instability of the elevator mode has a super-exponential growth. The subsequent nonlinear energy exchange between the triads also results in a statistical equilibrium of the elevator mode.

We gratefully acknowledge the financial support of the National Science Foundation (grants OCE-0092504 and OCE-0236304). We have greatly benefited from the referee's critical comments.

## Appendix

Previous phenomenological theories of equilibrium salt-fingering convection have been considered by Shen (1995), and Merryfield & Grinder (W. J. Merryfield & M. Grinder, Salt fingering fluxes from numerical simulations, unpublished manuscript, 2002, herein referred to as MG). Assuming round finger blobs with a characteristic length scale  $k^{-1}$ , vertical velocity  $W$ , and temperature and salinity anomalies  $\theta$ , and  $\sigma$ , in both papers, the authors arrive at essentially the same nonlinear (non-dimensional) system:

$$fk|W|W = Pr(\theta - \sigma) - Prk^2W, \quad (\text{A } 1)$$

$$fk|W|\theta = -W - k^2\theta, \quad (\text{A } 2)$$

$$fk|W|\sigma = -W/R - \tau k^2\sigma, \quad (\text{A } 3)$$

where  $f$  is an adjustable constant. MG suggest that the nonlinear terms correspond to enhanced dissipation of heat, salt and momentum, associated with the circulation and straining in a rising/descending blob. MG further point out that the above system ((A1)–(A3)) implies a cubic equation for the quantity  $fk|W| \equiv \lambda_{MG}$ , which is identical to the cubic (2.5) for the growth rate of linear fingers. It is further assumed that the most energetic fingers are realized, i.e.  $\lambda_{MG}$  is maximized with respect to  $k$ . This determines  $fk|W|$  and solving for  $\sigma$  (A3) gives the following salt eddy diffusivity

$$\frac{D_S}{K_T} = f^{-2} \frac{\gamma - R\tau}{R - \gamma}.$$

In order to close the above theories various *ad hoc* assumptions have been made, most notably the use of the same length scale for the flux convergence of heat, salt and momentum. The only parameter related to the final equilibrium state is the undetermined constant  $f$ , which is calibrated using the DNS. Compared to this, our theory goes a step further by using the secondary instability of the fingers to predict the mixing length and the corresponding salinity amplitude.

Mention should also be made of Kunze's (1987) work. He proposed that a secondary instability might limit the finger fluxes when the Froude number, based on the horizontally sheared finger velocity, becomes larger than 1.0. Using this criterion, however, he obtained flux formulae in which the fluxes decrease as  $R$  approaches 1.0, and which is opposite to the flux dependence inferred from DNS and suggested by observations (St Laurent & Schmitt 1999).

#### REFERENCES

- HOLYER, J. Y. 1984 The stability of long, two-dimensional salt fingers. *J. Fluid Mech.* **147**, 169–185.
- KUNZE, E. 1987 Limits on growing finite-length salt fingers: a Richardson number constraint. *J. Mar. Res.* **45**, 533–556.
- ST LAURENT, L. & SCHMITT, R. W. 1999 The contribution of salt fingers to vertical mixing in the North Atlantic Tracer Release Experiment. *J. Phys. Oceanogr.* **29**, 1404–1424.
- SCHMITT, R. W. 1979 The growth rate of super-critical salt fingers. *Deep-Sea Res.* **26A**, 23–40.
- SHEN, C. Y. 1995 Equilibrium salt-fingering convection. *Phys. Fluids* **7**, 706–717.
- STERN, M. E. 1960 The 'salt fountain' and thermohaline convection. *Tellus* **12**, 172–175.
- STERN, M. E., RADKO, T. & SIMEONOV, J. 2001 Salt fingers in an unbounded thermocline. *J. Mar. Res.* **59**, 355–390.
- STERN, M. E. & SIMEONOV, J. 2004 Amplitude equilibration of sugar–salt fingers. *J. Fluid Mech.* **508**, 265–286.